Two-Dimensional Contact and Noncontact Micromanipulation in Liquid Using an Untethered Mobile Magnetic Microrobot

Steven Floyd, *Student Member, IEEE*, Chytra Pawashe, *Student Member, IEEE*, and Metin Sitti, *Senior Member, IEEE*

***Abstract*—This paper presents the manipulation of microspheres under water by use of an untethered electromagnetically actuated magnetic microrobot (Mag-μBot), with dimensions $250 \times 130 \times 100$ μm^3. Manipulation is achieved by two means: contact and noncontact pushing modes. In contact manipulation, the Mag-μBot is used to physically push the microspheres. In noncontact manipulation, the fluid flow generated by the translation of the Mag-μBot is used to push the microspheres. Modeling of the system is performed, taking into account micrometer-scale surface forces and fluid drag effects to determine the motion of a sphere within a robot-generated fluid flow. Fluid drag models for free-stream flow and formulations for near-wall flow are both analyzed and compared with the experiments, in which pushing of two sphere sizes, i.e., 50 and 230 μm diameters, is characterized in a controlled, robot-generated flow. Dynamic simulations are provided using the developed physical models to capture this behavior. We find that the near-wall physical models are, in general, in agreement with the experiment, and free-stream models overestimate microsphere motion.**

***Index Terms*—Dynamics, manipulation planning, mechanism design, micro/nanorobots, telerobotics.**

I. Introduction

THE MANY methods for the manipulation of micrometer-scale objects can be classified into two fundamental categories: contact and noncontact manipulation. The distinction between the two is based upon the presence or absence of physical contact when manipulating micro-objects. In general, contact manipulation is preferred for the study of micro-objects that will not be damaged by any resulting contact forces. Noncontact methods are employed when manipulation forces must be comparatively low or if the micro-object is too fragile to be grasped by physical contact.

In most contact micromanipulation systems, a micrometer-scale end-effector, for example a microgripper, interacts with micro-objects. This end-effector is usually controlled by a multi degree-of-freedom macroscale positioning system. While such a system can have high dependability and repeatability, it can be complex, difficult to control, and expensive [1]. A simpler system that is cost effective and easier to control, with a micrometer-scale end-effector, can be a valuable alternative. Examples of systems demonstrating micromanipulation with a micrometer-scale end-effector are described in [2]–[4].

For any contact-based method, stiction between the end-effector and micro-object becomes significant at the micrometer-scale; this stiction makes releasing grasped micro-objects difficult. Methods to combat this problem can include using ice to form and break connections between end-effectors and micro-objects, vibrating the end-effector to release grasped micro-objects, employing a vacuum to selectively capture and release micro-objects, and using electrostatic attraction and repulsion to manipulate micro-objects [5], [6].

In noncontact manipulation methods, stiction between the micro-object and the manipulator is not a problem. Such methods include electrophoresis or dielectrophoresis [7], optical trapping [8], vibration of surfaces in [9] and [10], fluid-flow fields or bubbles in [11] and [12], and electromagnetic fields [13]. Many of these methods are performed in a fluid medium due to physical constraints of the manipulation method. If the micro-object is immersed in a fluid, there is little or no stiction with the surface; with a noncontact manipulator, the micro-object will not stick to it either. However, this limits applications to situations where the micro-object can be immersed in a fluid, which is not always the case. The low forces that are advantageous when applied to fragile micro-objects can be a negative aspect when a micro-object is relatively heavy or requires large contact forces to overcome the effects of friction.

One noncontact method of micromanipulation is utilizing fluid boundary layers to move micro-objects, which can be done in a fluid-flow field [14]. In many cases, it would be advantageous if no net fluid motion were necessary for manipulation, removing any requirements for channeling and maintaining flow.

In this paper, we propose a novel micromanipulation method using a micrometer-scale untethered magnetic end-effector, referred to as the magnetic microrobot (Mag-μBot). The manipulation occurs in a fluid immersed environment, which reduces

Manuscript received January 9, 2009; revised May 4, 2009. First published September 1, 2009; current version published December 8, 2009. This paper was recommended for publication by Associate Editor S. Hirai and Editor G. Oriolo upon evaluation of the reviewers' comments. This work was supported by the National Science Foundation CAREER Award Program under NSF IIS-0448042 and the NSF Graduate Research Fellowship.

S. Floyd and C. Pawashe (equally contributing co-first authors) are with the Department of Mechanical Engineering, Carnegie Mellon University, Pittsburgh, PA 15213 USA (e-mail: srfloyd@andrew.cmu.edu; csp@andrew.cmu.edu).

M. Sitti is with the Department of Mechanical Engineering and Robotics Institute, Carnegie Mellon University, Pittsburgh, PA 15213 USA (e-mail: sitti@cmu.edu).

This paper has supplementary downloadable multimedia material available at http://ieeexplore.ieee.org provided by the authors. This includes one mpeg-4 format video, which shows microrobot operation. This material is 39.7 MB in size.

Color versions of one or more of the figures in this paper are available online at http://ieeexplore.ieee.org.

Digital Object Identifier 10.1109/TRO.2009.2028761

the effects of stiction, and allows for the generation of fluid-flow fields as the Mag-μBot translates through the medium. These flow fields can exert forces on immersed micro-objects due to viscous drag, resulting in noncontact manipulation. Alternatively, the Mag-μBot can directly apply forces onto micro-objects via contact manipulation.

While limited to fluid operation, this system can be used to manipulate fragile items such as cells and durable items such as chemically functionalized microbeads. Micrometer-scale parts can be positioned and assembled into complex shapes and arrangements with this method, resulting in a microfactory. Being a tetherless microrobot, it can be included in lab-on-a-chip or other integrated and sealed microdevices.

Section II describes the system used to conduct the experiments, and explains in detail the process of both front (contact) and side (noncontact) pushing methods. The forces present on an immersed micro-object and the mathematical models used in this paper are described in Section III, along with estimates of the capabilities of the experimental system used. In Section IV, we describe the details of the simulation that is used to make estimates on the Mag-μBot's ability to push particles. Both simulated and experimental results are presented and described in Section V. Potential sources of error are discussed in Section VI, and conclusions with future works are presented in Section VII.

II. Magnetic Microrobot System

A rectilinear Mag-μBot with typical dimensions $250 \times 130 \times 100\ \mu\mathrm{m}^3$ is actuated by six independent electromagnetic coils, aligned to the faces of a cube approximately 11 cm on a side, with horizontal and vertical coils capable of producing maximum field strengths at the position of the Mag-μBot (see Fig. 1) of 3.0 and 2.3 mT, respectively. Imaging of the Mag-μBot and the workspace is accomplished by a camera (Sony XC-75) connected to a variable magnification microscope lens, providing a 4.6 mm $\times$ 3.4 mm field of view. Control of the electromagnetic coils is performed by a PC with a data-acquisition system at a control bandwidth of 1 kHz, and the coils are powered by custom-made electronic amplifiers. The Mag-μBot is made of neodymium–iron–boron (NdFeB, N42 grade), which is a hard magnetic material. To create the Mag-μBot, a magnetized piece of NdFeB was cut using a laser machining system (NewWave LaserMill).

Actuation of each Mag-μBot is accomplished by using two or three electromagnetic coils. One or more horizontal coils are first enabled (coil D in Fig. 1), causing the Mag-μBot to orient in the direction of the net magnetic field. The magnetic force exerted by the horizontal coils on the Mag-μBot is insufficient to translate it, due to friction and adhesion to the surface. Vertical clamping coils (coils C and F in Fig. 1) are enabled and pulsed using a sawtooth waveform, resulting in a nonuniform rocking motion of the Mag-μBot, which induces stick-slip motion across the surface. In general, the Mag-μBot's velocity increases with pulsing frequency, which is typically from 1 to 100 Hz, and can exceed velocities of 16 mm/s in air and 7 mm/s in water, as used in this study. The Mag-μBot is also capable of operating in fluids of viscosities less than about 50 cSt and can operate on a variety of smooth and rough magnetically inactive surfaces,

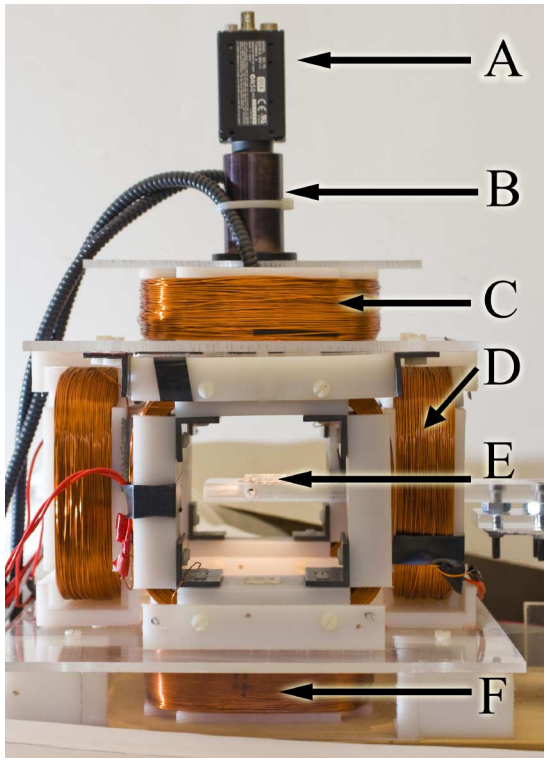

Fig. 1. Electromagnetic coil setup, where A is the camera for visual feedback, B is the microscope lens, C is the top coil, D is one of four upright coils that orients the Mag-μBot within the plane on the surface, E is the surface on which the Mag-μBot locomotes, and F is the bottom coil. The top and bottom coils are clamping coils, which provide a clamping force and a torque that pushes and orients the Mag-μBot toward the surface, respectively.

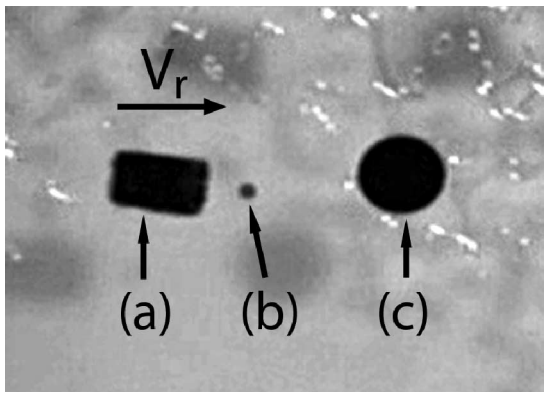

Fig. 2. Frame of a video of a $250 \times 130 \times 100\ \mu\mathrm{m}^3$ Mag-μBot (a) preparing to manipulate a 50-μm (b) and a 230-μm (c) PS-DVB microsphere in an underwater environment. V_r denotes the Mag-μBot's velocity. Video is available in the supplementary material.

provided that the adhesion between the Mag-μBot and surface is low. With an appropriate driving waveform, the Mag-μBot can be moved in steps down to about 5 μm.

Fig. 2 displays a frame of a video of a Mag-μBot manipulating 50- and 230-μm diameter polystyrene divinylbenzene (PS-DVB, Duke Scientific Inc.) microspheres underwater on a glass surface. In Fig. 3, five 50-μm-diameter PS-DVB spheres are arranged into a line by teleoperation. Further details on this system are explained in [15].

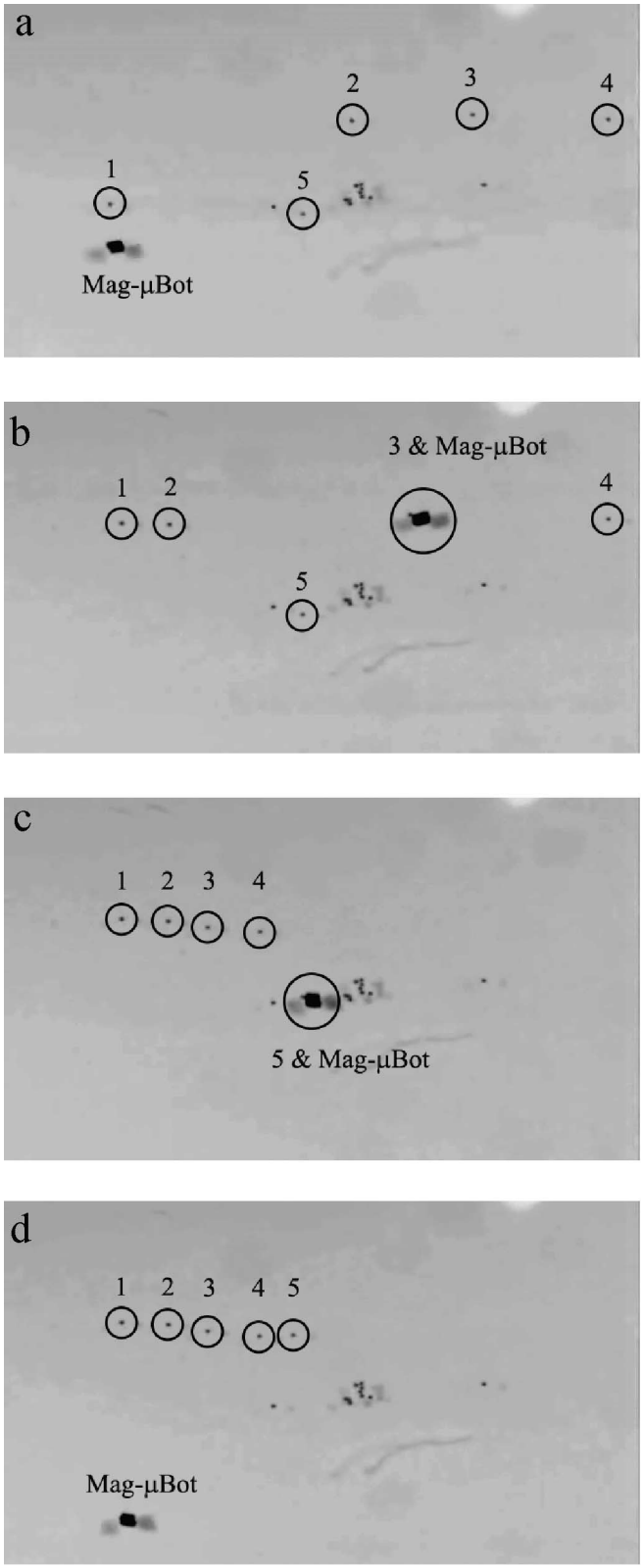

Fig. 3. Several frames from a movie of a teleoperated Mag-μBot pushing 50-μm diameter PS-DVB spheres across a glass surface under water. (a) Image of the five spheres selected by the user to be manipulated by the Mag-μBot. (b) Image after spheres 1 and 2 have been placed in a line, while sphere 3 is being pushed. (c) Image after the first four spheres have been placed in a line, while sphere 5 is being pushed. (d) Image after all five spheres have been placed in a line and the Mag-μBot has been returned to its initial position. Video is available in the supplementary material.

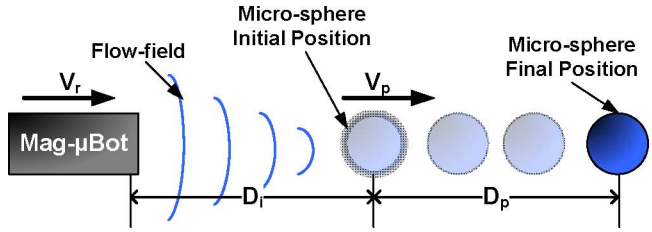

Fig. 4. Concept diagram showing a top view of front pushing of a microsphere by a Mag-μBot. V_r and V_p denote the Mag-μBot and particle velocities, respectively. D_i is the interaction distance between the Mag-μBot and the sphere, and D_p is the displacement of the sphere. The sphere and Mag-μBot both move from left to right.

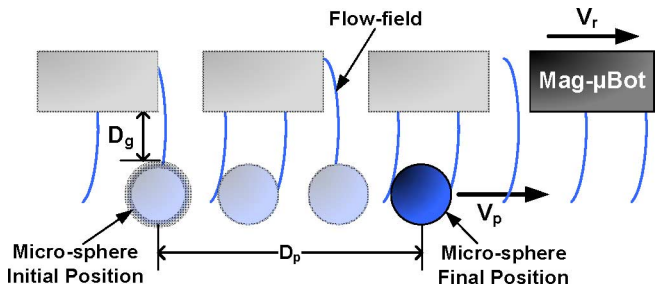

Fig. 5. Concept diagram showing a top view of side pushing of a microsphere by a Mag-μBot. V_r and V_p denote the Mag-μBot and particle velocities, respectively. D_g is the initial gap distance between the Mag-μBot and the sphere, and D_p is the displacement of the sphere. The sphere and Mag-μBot both move from left to right.

A. *Micro-Object Manipulation*

The Mag-μBot is capable of moving micro-objects underwater by contact or noncontact manipulation. As the Mag-μBot traverses in the fluid, flow fields are generated, which interact with other objects in the fluid. Fig. 4 displays the process of a Mag-μBot pushing a microsphere from the front. First, the flow field generated by the Mag-μBot becomes significant at an interaction distance D_i and displaces the sphere a distance D_p before the Mag-μBot comes into contact with the sphere. Afterward, the Mag-μBot may push the sphere further by contact manipulation until contact is lost.

In Fig. 5, the process of a Mag-μBot pushing a microsphere from the side is explained, which results in noncontact manipulation. D_g is the initial gap distance between the Mag-μBot and the sphere, and D_p is the displacement of the sphere caused by the induced flow fields as the Mag-μBot passes by.

III. Modeling

When the Mag-μBot manipulates a microsphere, two interactions are of importance: 1) surface interactions, which include the effects of adhesion and friction between the microsphere and the substrate; and 2) fluid interactions, which include the induced drag force on the microsphere. This section provides theoretical background on these interactions, and conditions are developed on the Mag-μBot's ability to manipulate microspheres.

TABLE I
PROPERTIES OF MATERIALS

Material	Surface Energy (γ) $[\mathrm{mJ}\cdot\mathrm{m}^{-2}]$	Young's Modulus (E) [GPa]	Poisson Ratio (ν)
Glass	83-280 [21]–[24]	70	0.25
Polystyrene	33-40 [18], [25]	3.2	0.35
Water	72.3	-	-

A. Adhesion at the Micrometer-Scale

When pulling two objects at the micrometer-scale apart from one another, a nonzero pull-off force arises. This force is due to a combination of van der Waals interactions, capillary effects, and electrostatic charging [16]. Capillary forces can be removed or neglected if the humidity is kept below 10%. Electrostatic effects are usually small compared with van der Waals due to the low dielectric strength of air [17] and can also be neglected. To determine what the pull-off force for separating two materials 1 and 2 is, the work of adhesion W_{12} must be determined for the pair utilizing their intrinsic surface energies γ_1 and γ_2, respectively [18], [19]

$$W_{12} = \gamma_1 + \gamma_2 - \gamma_{12} \approx 2\sqrt{\gamma_1\gamma_2}. \tag{1}$$

Adhesion modeling for microparticle and nanoparticle manipulation is discussed in [20], where the Johnson–Kendall–Roberts (JKR), Deraguin–Muller–Toporov (DMT), and Maugis–Dugdale (MD) models are explained. To determine which of the three is most appropriate to use, a dimensionless parameter λ, which is often called the elasticity parameter, is introduced

$$\lambda = \left(\frac{8R_e W_{12}^2}{\pi h^3 K^2}\right)^{\frac{1}{3}} \tag{2}$$

$$K = \frac{4}{3}\left(\frac{1-\nu_1^2}{E_1} + \frac{1-\nu_2^2}{E_2}\right)^{-1} \tag{3}$$

$$R_e = (R_1^{-1} + R_2^{-1})^{-1} \tag{4}$$

where R_e is the effective radius of contact for two objects of radii R_1 and R_2, $h = 0.165$ nm is a typical separation distance between the points of contact for the two materials, and K is the equivalent elastic modulus of contact, based upon each material's Young's modulus (E_1 and E_2) and Poisson ratio (ν_1 and ν_2) [19].

The range of possible pull-off forces P is curtailed, and any value of λ will result in a P that falls within the range of

$$\frac{3}{2}\pi R_e W_{12} \le P \le 2\pi R_e W_{12} \tag{5}$$

where the exact value of P can be determined based upon the value of λ. Hence, with only information on the surface energy of the material, an upper limit on P can be determined.

Values of several relevant properties for materials used in this paper are given in Table I.

Due to the wide range of possible surface energies for glass given in Table I, there is a large range of pull-off forces that can potentially exist for a polystyrene sphere of a given diameter contacting glass. It will be shown that this large variance is not important when the system is immersed in water.

B. Adhesion in Fluid

When operating completely within a fluid, such as water, the capillary and electrostatic contributions to the adhesive pull-off force can be neglected. The van der Waals adhesion can be determined by taking into account the interactions with the fluid medium [19]

$$W_{132} = W_{12} + W_{33} - W_{13} - W_{23} \tag{6}$$

where the subscripts 1 and 2 correspond to the solid materials, and 3 corresponds to the fluid medium.

In this case, the resulting work of adhesion can be either positive or negative. Negative values imply the two surfaces repel each other and minimize their energy by contacting the fluid, creating a thin fluid layer between them. For the range of surface energy values of both polystyrene and glass presented in Table I, the corresponding range of immersed work of adhesion is $-44.8\ \mathrm{mJ}\cdot\mathrm{m}^{-2} < W_{132} < -3.1\ \mathrm{mJ}\cdot\mathrm{m}^{-2}$, which is strictly negative. Hence, in the experiments, there is always repulsion between the glass substrate and the microspheres.

The implication of this water lubrication layer on the dynamics of particle manipulation is that any friction or adhesion forces caused by the surface can be ignored; microsphere motions are solely due to fluid interactions.

C. Fluid Boundary Layers

Near an object with a nonzero velocity relative to the fluid medium in which it is immersed, there exists a volume of fluid wherein viscous effects are significant. Fluid closer to this object moves at higher velocities than fluid farther away. At some distance demarcated by a theoretical boundary layer, the difference between the local velocity of the perturbed fluid and the unperturbed fluid is less than 1% of the maximum difference between the two. For example, if a Mag-μBot was traveling at 2.0 mm/s, then the 1% boundary layer encompasses the fluid volume surrounding the Mag-μBot moving at or greater than 1% of this maximum velocity or 20 μm/s. Outside this boundary layer, fluid motion is nearly inviscid, and the effects of the Mag-μBot's presence are minimized. Within this boundary layer, fluid flow is deflected from the motion it would have if the Mag-μBot was not present [26].

For the purposes of this paper, we are interested only in the fluid flow around the Mag-μBot that can cause sufficient viscous drag to move a microsphere at a velocity that can be conveniently perceived by our equipment. Once the fluid flow around the Mag-μBot is determined, a critical fluid-flow field (CF^3) based upon this velocity can be found. If we assume a sphere is moving at the same speed as the fluid, note that the camera pixel size is approximately 7 μm and the camera frame rate is 30 frames/s and expect motion of an object can be unambiguously detected to within half a pixel of displacement, then a reasonable CF^3 would be the volume of fluid moving at $0.5 \times 7\,\mu\mathrm{m} \times 30\,\mathrm{Hz} \approx 0.1\,\mathrm{mm/s}$. For the range of velocities used in this paper, this CF^3 is much smaller than the 1% boundary layer, which is shown

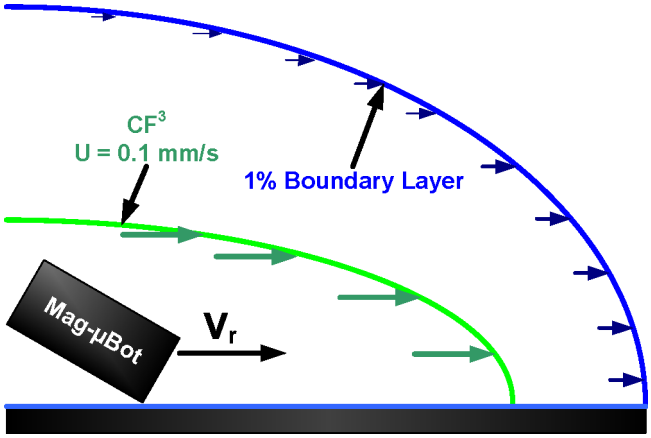

Fig. 6. As the Mag-μBot translates through the fluid, it causes local fluid motion demarcated by an outer boundary layer, where the fluid returns to within 1% of its unperturbed state. The CF^3 indicates the fluid boundary where the volume enclosed has a velocity high enough to cause a micro-object to be accelerated visibly. The generated boundary layer by the Mag-μBot is much larger than the CF^3 for the range of velocities used in this paper.

schematically in Fig. 6. While smaller displacements can be detected using subpixel image analysis techniques, leading to a larger CF^3, we believe the value of $0.1\ \mathrm{mm/s}$ is sufficient to test the validity of the fluid drag models in noncontact pushing scenarios.

D. Viscous Drag

The fluid-flow field generated by a translating Mag-μBot exerts a viscous drag force on nearby microspheres. This drag force can be found using the empirically derived Kahn–Richardson formulation for a sphere F_{KR}, which is valid for a large range of Reynolds numbers ($0 < Re < 10^5$) [27]

$$Re = \frac{2R\rho}{\mu}U$$

$$F_{\mathrm{KR}} = \pi R^2 \rho (U - V_p)^2 \times \left(1.84 Re^{-0.31} + 0.293 Re^{0.06}\right)^{3.45} \quad (7)$$

where the Reynolds number Re is a function of the sphere's radius R, the fluid velocity U, the fluid density ρ, and the dynamic viscosity of the fluid μ. To find the force on the sphere, the difference between the fluid's velocity U and the sphere's velocity V_p is used.

For the small range of Mag-μBot velocities used in this study, this force can be simplified by using the viscous drag equation for a sphere at low Reynolds number [26] and still provide results to within 2.5% of the Kahn–Richardson model

$$F_{\mathrm{drag}} \approx 6\pi\mu R(U - V_p). \quad (8)$$

Both of these fluid models tend to overestimate the forces exerted on an object that is very near a nontranslating wall. Because of the no-slip condition that exists at the wall, there must exist a nonuniform flow, resulting in a shear flow across an object. For the case of a spherical object near a wall, this results in a rotation and a lift force normal to the wall applied to the sphere. Correction factors for (8), plus the inclusion of forces induced by rotation, which were first calculated by Goldman *et al.* [28], [29], can be used to determine the near-wall fluid forces (F_G)

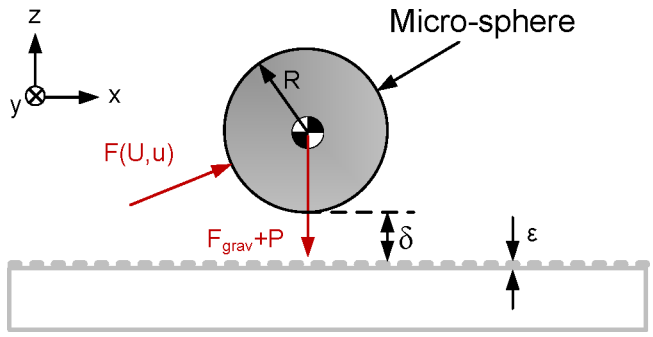

Fig. 7. Free body diagram of the forces on a submerged sphere during manipulation. $F(U, V_p)$ is the fluid drag force, F_{grav} is the effective force of gravity, and P is the force due to surface adhesion. δ is the distance from the bottom of the sphere to the surface, and ϵ denotes a surface roughness. The y-axis is into the page.

$$F_G = 6\pi\mu R \times \left(U_{\mathrm{ip}} F^*_{\mathrm{shear}} + V_{p,\mathrm{ip}} F^*_{\mathrm{trans}} + \Omega R F^*_{\mathrm{rot}}\right) \quad (9)$$

$$F^*_{\mathrm{shear}} = 1 + 0.7005\frac{R}{h}$$

$$F^*_{\mathrm{trans}} = \frac{8}{15}\ln\left(\frac{\delta+\epsilon}{R}\right) - 0.9588$$

$$F^*_{\mathrm{rot}} = -\frac{2}{15}\ln\left(\frac{\delta+\epsilon}{R}\right) - 0.2526$$

where U_{ip} is the in-plane fluid velocity at the sphere's center (i.e., in the x- and y-axes in Fig. 7), $V_{p,\mathrm{ip}}$ is the in-plane velocity of the sphere, and Ω is the angular velocity of the sphere's rotation, where the axis of rotation is assumed parallel to the plane. Also, $h = R + \delta + \epsilon$ is the distance from the center of the sphere to the no-slip boundary condition, which is dependent upon δ, the distance between the edge of the sphere and the ground, and $\epsilon \approx 25\,\mathrm{nm}$, which is the measured combined characteristic roughness of the two surfaces, shown schematically in Fig. 7. Each of the logarithm terms in (9) is appropriately bounded, i.e., $F_{\mathrm{trans}} \leq -1$, $F_{\mathrm{rot}} \geq 0$. The angular velocity can be related to the translational velocity and the distance from the wall by fitting a curve to the numerical results of [28] and bounding it to $0 \leq \Omega \leq 0.5676\, V_p/R$, which results in

$$\Omega = (-2.375 \times 10^{-6} e^{12.05R/h} + 1.025 e^{-.1438R/h})\frac{V_p}{R}. \quad (10)$$

In addition, Ω can induce a lift force in the sphere in the z-direction. This lift force was found to be less than 2% of the sphere's buoyant weight and is ignored in the simulations.

These models assume the velocity distribution across the sphere is small, which may or may not be true in the case of a Mag-μBot manipulating micro-objects. For the purposes of theoretical calculations used in this paper, the volume averaged fluid velocity $\bar{U}(t)$ that exists in the absence of the sphere can be used instead of the fluid velocity at the center of the sphere.

With a known flow field $U(x, y, z, t)$, this can be determined by

$$\bar{U}(t) = \int_V U(x, y, z, t) dV \tag{11}$$

where V is the volume of the sphere being pushed by the fluid.

Both the Kahn–Richardson and Goldman force models are used throughout this paper to estimate fluid forces applied parallel to the ground plane. For forces in the z-direction, the Kahn–Richardson force is used in both cases. In addition, a gravitational force acting upon the buoyant mass $F_{\text{grav}} = (\rho_p - \rho)Vg$, with ρ_p being the density of the immersed object and g being the acceleration due to gravity, is included among the forces in the z-direction. A free body diagram of a microsphere with relevant geometry is shown in Fig. 7. The equations of motion used in the simulations are

$$m\ddot{x} = [F_G(U_x, V_{p,x}) \text{ or } F_{\text{KR}}(U_x, V_{p,x})] + F_{Sx} \tag{12}$$

$$m\ddot{y} = [F_G(U_y, V_{p,y}) \text{ or } F_{\text{KR}}(U_y, V_{p,y})] + F_{Sy} \tag{13}$$

$$m\ddot{z} = F_{\text{KR}}(U_z, V_{p,z}) - F_{\text{grav}} + F_{Sz} \tag{14}$$

where U_i is the component of the flow field in the ith direction, $V_{p,i}$ is the component of the sphere velocity in the ith direction, and $F_{Si} = -kd_i$ is a spring force applied in the ith direction when the sphere attempts to penetrate a stiff surface, such as the Mag-μBot, to a depth d_i. The spring stiffness $k = K(\pi a^2/R) \approx 0.02$ N/m is based upon an elastic cylinder assumption, and utilizes a Hertzian contact model (without adhesion) to determine the contact radius $a = (RF_{\text{grav}}/K)^{1/3}$ due to gravity within the fluid medium for a 50-μm sphere [19]. Using (7), the Reynolds number for the two sphere sizes used ranges from ≈ 0.005 for the 50-μm sphere moving at 0.1 mm/s to ≈ 0.4 for the 230-μm sphere moving at 1.6 mm/s. This range of Reynolds numbers approaches unity; therefore, inertial effects should not be neglected. Thus, accelerations are incorporated into the equations of motion [26].

E. Manipulation Capabilities

Using the information in the previous sections, logical limits can be determined on the ability of a Mag-μBot to perform either contact or noncontact pushing based upon the forces that must be overcome. Within a fluid medium, there exists a minimum lateral force $F_{\min}$ to move an object

$$F_{\min} \approx \mu_f \left[2\pi R W_{132} + (\rho_p - \rho)Vg\right] \tag{15}$$

where μ_f is the immersed friction coefficient between the surface and the object.

If $F_{\min} \leq 0$, pushing of the object is guaranteed; however, displacements incurred may be too small to detect if exerted forces are too low or object inertia is too high.

The maximum possible forces exerted in contact mode by the Mag-μBot can be roughly approximated by the maximum lateral magnetic force that can be applied to the Mag-μBot, approximately 52 nN [15]. Using (8), the maximum force exerted on a 100-μm diameter sphere by a Mag-μBot traveling at 2 mm/s is approximately 1.7 nN in noncontact mode. Contact forces are much higher than noncontact forces, but neither is exceptionally large. For example, the effective weight of a steel sphere 100 μm in diameter immersed in water is approximately 35 nN. Assuming negligible adhesion, a steel sphere with an immersed coefficient of friction of $\mu_f = 0.1$ can only be pushed in noncontact mode if it is less than 70 μm in diameter and in contact mode if it is less than 246 μm in diameter.

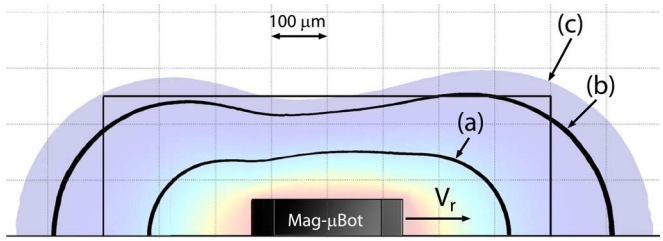

Fig. 8. Top-down view of the fluid flow is shown in color for a Mag-μBot traveling towards the right at a velocity $V_r = 1.6$ mm/s, at a distance 100 μm above the ground. Only half of the Mag-μBot is simulated to reduce simulation time, and is valid due to symmetry. The CF^3 boundaries at 0.1 mm/s are shown for different translational velocities, where the boundary (a) is when $V_r = 0.35$ mm/s, (b) is when $V_r = 1.1$ mm/s, and (c) is when $V_r = 1.6$ mm/s. The grid spacing shown is 100 μm.

For this reason, experiments are performed using PS-DVB particles, which are nearly neutrally buoyant (density $\rho_{\text{PS}} = 1060\,\text{kg/m}^3$). This, combined with a negative work of adhesion, makes them ideal for determining to what extent both contact and noncontact manipulation can be performed using the Mag-μBot and the accuracy of models and simulations used in this paper.

IV. Simulation

To estimate the ability of the Mag-μBot to push the microspheres using noncontact methods, the fluid motion caused by the Mag-μBot's translation was calculated using COMSOL Multiphysics: a finite-element package. The Navier–Stokes equations for incompressible flow [26] are solved, which results in the fluid velocity at every point in the simulation space. The Mag-μBot is modeled as remaining stationary at an angle of 22.5° to the surface (an approximate average angle of the Mag-μBot as it translates), and the fluid flows over the Mag-μBot at its translational velocity, corresponding to the velocities used in the experiments. The ground is treated as a moving wall with tangential velocity equal to the flow velocity, while all other external bounding surfaces have a symmetry boundary condition applied. This allows no fluid flow across these boundaries; it is only tangential to them. Along all faces of the Mag-μBot, a no-slip boundary condition was used.

A. CF^3 Distribution

Once a fluid-flow solution is determined, the flow field is plotted as $U(x, y, z) - v_d$, where v_d is the default fluid velocity, i.e., the experimentally determined Mag-μBot translational velocity. This results in a plot of the fluid motion in a reversed reference frame, where the Mag-μBot is translating in a stagnant fluid. In Figs. 8 and 9, the 0.1 mm/s CF^3 is shown for a top-down and side view, respectively, for Mag-μBot velocities of 0.35, 1.1, and 1.6 mm/s (as used in the experiments).

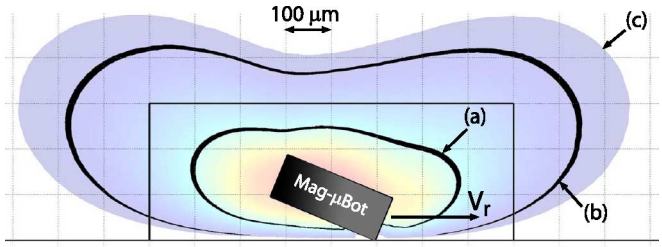

Fig. 9. Side view of the fluid flow is shown in color for a Mag-μBot traveling towards the right at a velocity $V_r = 1.6$ mm/s, taken at a distance 100 μm from the centerline of the Mag-μBot. The CF^3 boundaries at 0.1 mm/s are shown for different translational velocities, where the boundary (a) is when $V_r = 0.35$ mm/s, (b) is when $V_r = 1.1$ mm/s, and (c) is when $V_r = 1.6$ mm/s. The grid spacing shown is 100 μm.

As the Mag-μBot's velocity increases, the 0.1 mm/s CF^3 increases in size. At 0.35 mm/s, the boundary layer extends approximately 200 μm in front of and behind the Mag-μBot, whereas at 1.6 mm/s, the boundary layer extends approximately 600 μm on both the front and the back, shown in Fig. 8. In addition, the 0.1 mm/s CF^3 extends to the sides of the Mag-μBot for greater distances at higher speeds. Also, the CF^3 first increases and then decreases in size as the distance from the ground increases, as shown in Fig. 9.

B. Sphere Motion

Once the solution to the flow fields is determined within the modeling space, MATLAB is used to simulate the motion of a microsphere through the flow field. The sphere is initially positioned in front of the Mag-μBot at a lateral distance D_g from the Mag-μBot's edge sufficiently far in front of the Mag-μBot that the CF^3 does not initially interact with the sphere. Both the Kahn–Richardson and Goldman force models are used to determine the sphere's acceleration using (12)–(14) based upon its location and the local fluid velocities. The path a sphere placed into the flow would take is computed using a Runge–Kutta solver (ODE23). Once the sphere has passed completely through the CF^3, the difference between the sphere's end position and the end position of an undisturbed sphere, i.e., one traveling at the free stream velocity, is used to determine the displacement D_p of the sphere due to the effects of the Mag-μBot passing.

Fig. 10 shows the paths 50-μm spheres take in the simulation, depending on D_g. Both in the experiments and in the simulations, the flow field generated by the moving Mag-μBot causes spheres to be pushed away from the Mag-μBot as it approaches. As the Mag-μBot passes the sphere, it is pulled toward the Mag-μBot's wake. The final relative displacement of the microspheres can have components both parallel and perpendicular to the motion of the Mag-μBot, but only parallel motion is taken into account when determining the D_p.

C. Sphere Size

Within the simulations, the displacements of a range of microsphere sizes is examined, as shown in Fig. 11, for a Mag-μBot traveling at 1.6 mm/s, using side pushing with $D_g = 0$. From this figure, it can be seen that the Khan–Richardson formulation predicts much larger displacements than the Goldman force model.

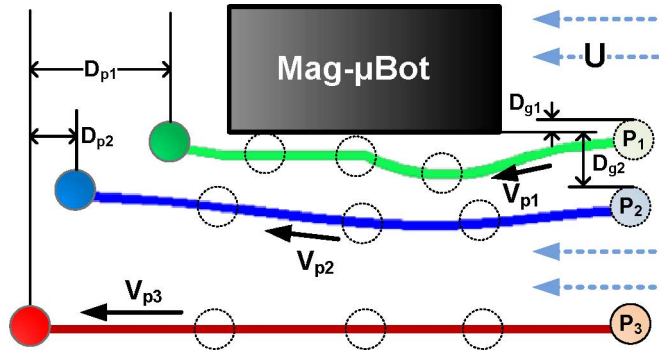

Fig. 10. Simulation displaying the path a microsphere takes when placed in a flow $U = 1.6$ mm/s with a fixed Mag-μBot. P_1 is a sphere that begins close to the Mag-μBot, P_2 is a sphere further away from the Mag-μBot, and P_3 is a sphere in a flow without the Mag-μBot. D_{p1} and D_{p2} are the effective displacements of P_1 and P_2, respectively. D_{g1} and D_{g2} are the initial gap distances to the Mag-μBot from P_1 and P_2, respectively; $D_{g3} = \infty$ for P_3. V_{p1}, V_{p2}, and V_{p3} denote the respective sphere's velocities.

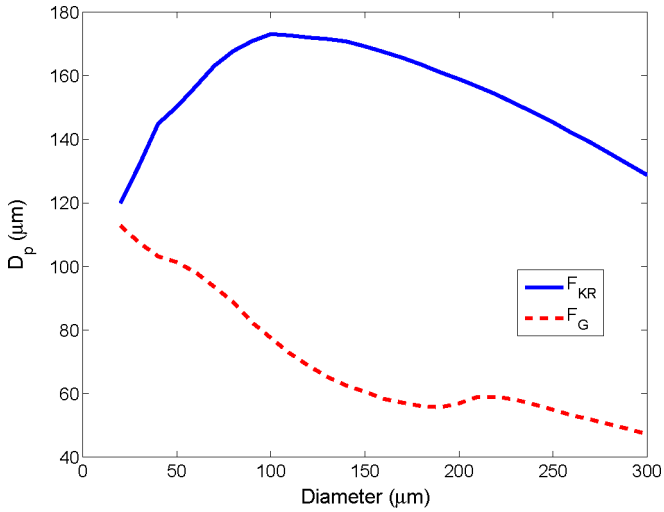

Fig. 11. Simulated particle travel distance in side pushing versus microsphere radius using both the Kahn–Richardson (F_{KR}) and Goldman (F_G) force models for a Mag-μBot traveling at 1.6 mm/s.

V. Experimental Results

In the experiments, 50 and 230-μm diameter PS-DVB microspheres were used. Three Mag-μBot velocities were employed: 0.35, 1.1, and 1.6 mm/s, which are achieved by specifying the frequency of magnetic field pulsing (5, 20, and 50 Hz, respectively). Multiple trials were performed to attain an average and error bounds for the results. During each experiment, a video of the Mag-μBot motion was recorded and post-processed. A conversion ratio from the video image to real-world distances was empirically determined by counting the pixels across a known length and found to be approximately 7.2 μm/pixel. All estimates on position are accurate to within 2 pixels, or about 14 μm.

Two types of pushing experiments were performed: front pushing (see Fig. 4) and side pushing (see Fig. 5). For front pushing, the Mag-μBot was positioned far from the sphere and aligned so that the sphere was nearly in the center of the Mag-μBot's travel path. The Mag-μBot then approached the sphere and pushed it by direct contact. Both the interaction distance (D_i) and the noncontact displacement (D_p) of the sphere that occurred prior to the Mag-μBot contacting the sphere were recorded as a function of Mag-μBot velocity for both sphere sizes. The total sphere displacement was not recorded; in perfect front pushing, the sphere will move along with the Mag-μBot indefinitely.

For side pushing, the initial gap distance (D_g) between the sphere and the Mag-μBot's closest edge was recorded. The total displacement (D_p) of each sphere as a function of Mag-μBot velocity was recorded for both sphere sizes. Several frames from a movie demonstrating side pushing are shown in Fig. 12.

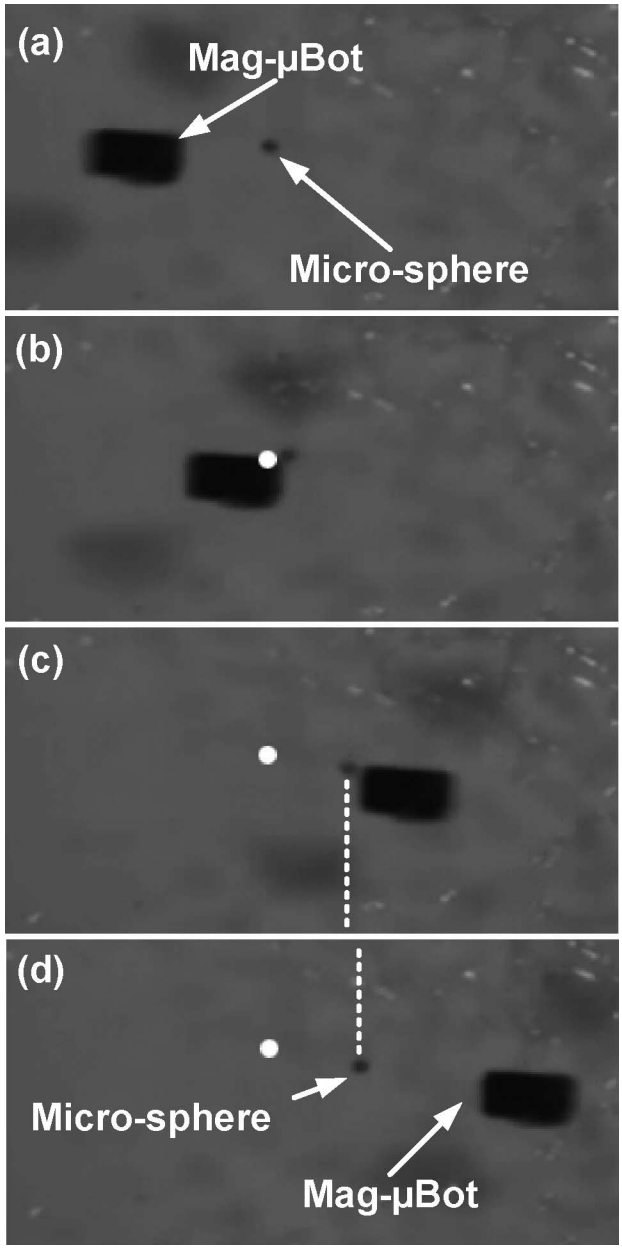

Fig. 12. Several frames from a movie of a teleoperated Mag-μBot pushing a 50-μm microsphere across a glass surface underwater. The sphere's initial position is shown as a white dot. In (a) the Mag-μBot approaches the sphere and begins to observably perturb it. In (b), the Mag-μBot is in close proximity to the sphere, and some noncontact displacement has occurred. In (c), the Mag-μBot passes the sphere as its velocity is higher than that of the sphere; any contact is completely lost. In (d), the final displacement of the sphere is shown, where the Mag-μBot is past the point where it can affect the sphere. Some additional sphere displacement has occurred due to the wake of the Mag-μBot. Dashed white lines are shown in (c) and (d) to illustrate the noncontact displacement which occurs when the particle is behind the Mag-μBot.

A. *Front Pushing*

For front pushing experiments, the sphere was approached from a distance greater than the estimated CF^3 extent while trying to maintain it at the center of the Mag-μBot's path of travel. Approximately 75% of the spheres were pushed via the front pushing method in this way, while 25% moved to the side and were pushed via the side pushing method.

The simulated and experimental interaction distances, D_i, for front pushing are shown for three velocities in Fig. 13. For the simulated D_i, the extent the CF^3 precedes the Mag-μBot at a distance from the substrate equal to the radii of the two spheres was used. It can be seen that there is good agreement between the CF^3 extent and the experimentally determined interaction distances. For higher velocities, while it may seem that the CF^3 distance overestimates D_i, it should be noted that the Mag-μBot is moving at a rate of approximately 50 μm per frame, which is a speed that can easily shift the experimental results downward by up to 50 μm if motion initially occurs between frames.

In all cases, the 50-μm sphere is less affected than the 230-μm sphere. This is likely due to the fact that the fluid velocity decreases as it approaches the wall, shown in Fig. 9, putting smaller spheres in a lower velocity fluid field relative to the motion of the Mag-μBot.

Before any contact is made with the sphere in front pushing, it will displace from its initial position due to the CF^3 preceding the Mag-μBot. The total simulated and experimental displacement, D_p, caused by this fluid force in front pushing is displayed in Figs. 14 and 15 for 50- and 230-μm particles, respectively. It can be seen that the two fluid force solutions bound the experimental results for both particle radii and are good predictors.

For both sphere diameters, the Goldman force model appears closer than the Kahn–Richardson model in predicting microsphere motion, where the latter model overestimates sphere motion by nearly a factor of two.

B. *Side Pushing*

For side pushing, D_g, as shown in Fig. 5, is used as the independent variable and can be negative if the sphere initially obscures a portion of the Mag-μBot's path. Side pushing is a combination of noncontact and contact pushing for spheres that are initially close to the Mag-μBot's path and is purely

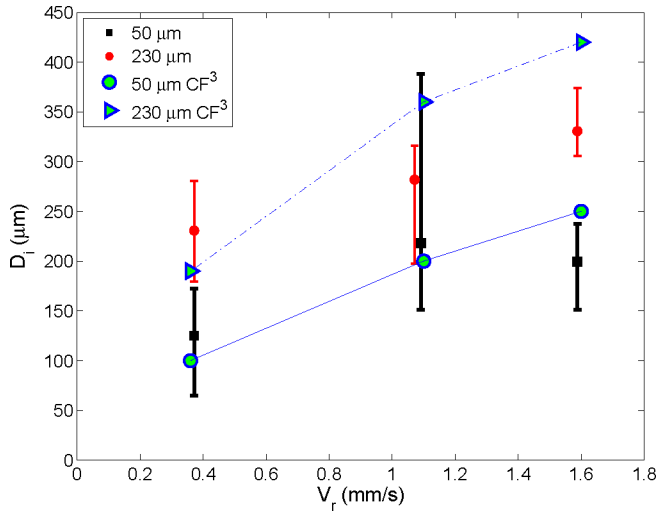

Fig. 13. Interaction distance (D_i) during front pushing for 50- and 230-μm diameter particles at three Mag-μBot velocities (V_r) compared with calculated CF^3 velocities. Error bars include three to six data points. Some data slightly shifted to improve readability.

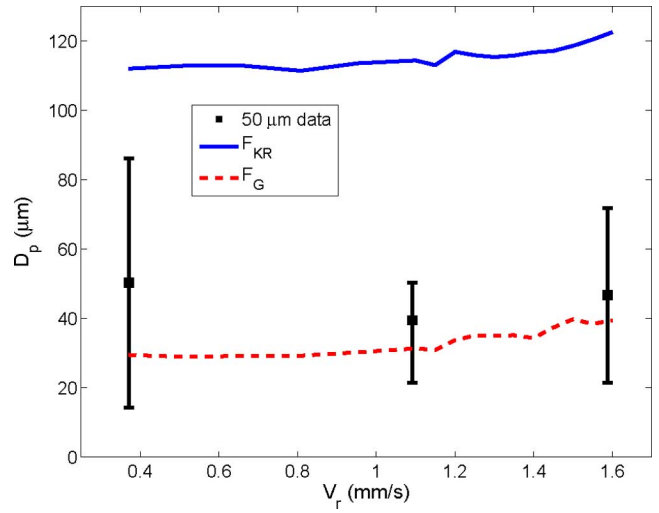

Fig. 14. Distance (D_p) traveled by a 50-μm diameter sphere before any contact with the Mag-μBot occurs for several Mag-μBot velocities (V_r). Error bars include three to six data points.

noncontact manipulation for spheres placed further away, as shown in Fig. 10.

As in the case of front pushing, the effect of V_r on D_p was found to be negligible in side pushing from the simulations. In Figs. 16 and 17, the effect of D_g on D_p is shown in both the simulations and the experiments with 50- and 230-μm spheres, respectively. For the 50-μm spheres, results for the higher Mag-μBot velocities and larger values of D_g more closely resemble the simulated predictions, and are largely independent of Mag-μBot speed. The lower velocity results with a small initial gap show much larger displacements than predicted by the simulation. This may be due to aspects of the flow that are not being modeled, such as the intermittent motion of the Mag-μBot, which translates using stick slip locomotion.

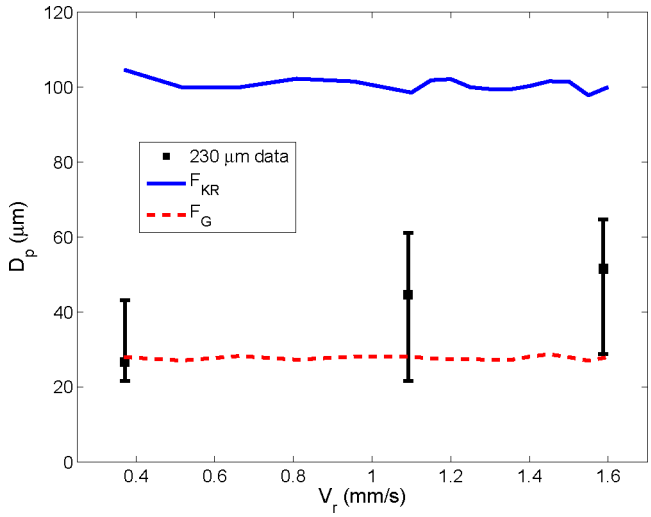

Fig. 15. Distance (D_p) traveled by a 230-μm diameter sphere before any contact with the Mag-μBot occurs, for several Mag-μBot velocities (V_r). Error bars include three to six data points.

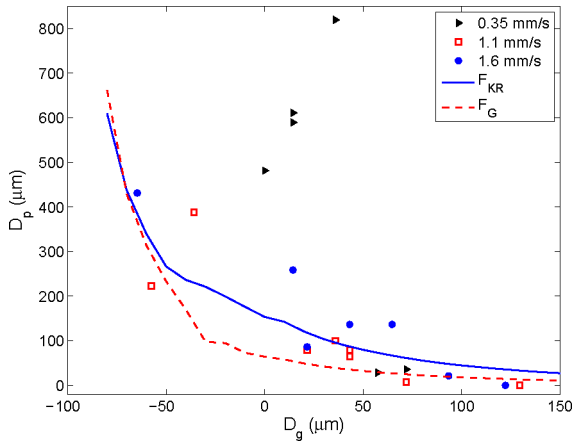

Fig. 16. Simulated and experimental 50-μm sphere travel distances (D_p) in side pushing versus initial gap distance (D_g) for three Mag-μBot velocities. In the simulations, both the Kahn–Richardson (F_{KR}) and Goldman (F_G) force models are shown for $V_r = 1.6$ mm/s.

For 230-μm spheres, the experimental data more closely resembles the simulation corresponding to the Goldman force estimates. This can be attributed to the fact that for a sphere contacting the ground only by its asperities ($\delta \to 0$), the ratio of ϵ/R will be much smaller for larger radii, and any wall effect will be proportionally larger, as seen in (9). The discontinuities seen in both the Kahn–Richardson and Goldman force models at $D_g \approx -25\,\mu$m are due to the transitions from a purely noncontact pushing to a contact pushing method, which is similar to P_1 in Fig. 10. Even without any simulated friction at the contact point, contact with the Mag-μBot can affect the translation distance of the spheres.

VI. Error Analysis

As mentioned in Section V-A, one potential source for error in determining the interaction distance is the Mag-μBot's velocity. At higher velocities, the Mag-μBot approaches the sphere at

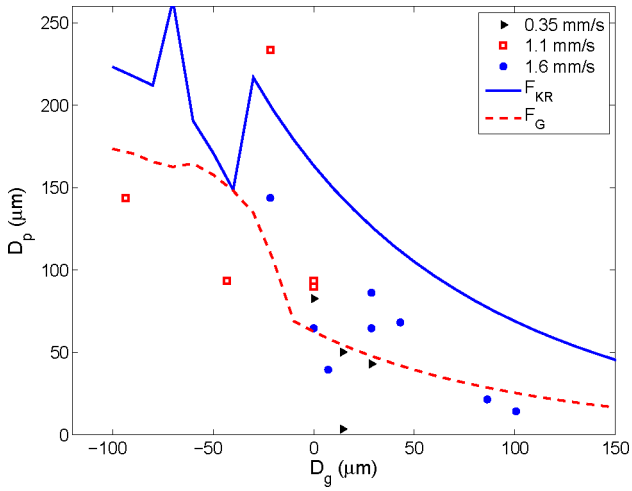

Fig. 17. Simulated and experimental 230-μm sphere travel distances (D_p) in side pushing versus initial gap distance (D_g) for three Mag-μBot velocities. In the simulations, both the Kahn–Richardson (F_{KR}) and Goldman (F_G) force models are shown for $V_r = 1.6$ mm/s.

upwards of 50 μm per frame. This can cause an underestimation of D_i on the order of 50 μm due to the rapidly changing CF[3].

The distribution of values associated with the recorded motion of the 50-μm spheres are in general larger than those associated with the 230-μm spheres. This is likely due to the difference in their Reynolds numbers. Because the Mag-μBot has a periodic rocking motion as it travels, it can create large instantaneous flow velocities and vortices. The larger importance of inertia and gravity for the 230-μm sphere makes it more immune to these effects, leading to smaller distributions in measured velocity.

To determine the fluid-flow field, the Mag-μBot was modeled in COMSOL at a constant angle of 22.5°. In reality, the Mag-μBot oscillates as it translates due to its stick-slip motion, and both oscillation and translation are periodic, not constant. These oscillations can cause fluid to be squeezed out of the backside of the Mag-μBot, potentially pushing smaller particles laterally away from the Mag-μBot, or vertically away from the ground. If smaller particles were pushed laterally, they may travel shorter distances than predicted, because they would be farther from the Mag-μBot, and in a slower relative flow field. If those particles were instead pushed vertically into a larger Mag-μBot-induced flow field, they may be pushed further than the simulation predicts. These effects would not be expected for larger particles, which are more affected by gravity and inertia, and are less likely to be moved by any squeeze flow. This could potentially explain the discrepancy between simulation and experiment for the 50-μm particles when the Mag-μBot is moving at 0.35 mm/s, corresponding to a 5-Hz oscillation frequency. At low frequencies, the intermittent motion of the Mag-μBot is least like the constant flow model used in the simulations.

VII. Conclusion and Future Work

In this study, the ability of an untethered magnetic microrobot to manipulate microspheres was demonstrated and analyzed. Both contact and noncontact methods were shown to be viable manipulation techniques. A computer simulation was used to estimate the displacement caused by both front and side pushing, which included a numerical solution to the flow field created by the translating Mag-μBot. The results of this simulation, which used two different force models based upon the fluid flow, were found to place reasonable bounds on the amount of observed motion, with the Goldman near-wall force model better predicting experimental results.

Future work will cover a more comprehensive fluid model, which will include the effect of the Mag-μBot's oscillatory motion. By examining high speed video, the Mag-μBot's orientation and velocities can be determined, which can be used to create a set of numerical fluid-flow solutions. As the particle translates, the local fluid velocity can be interpolated between these solutions as a function of time. Additionally, we would like to expand this work to include generic micro-object shapes, both in the simulations and in the experiments, which means introducing the effects of rotation into the model. Afterward, the microrobotic system can be improved to include autonomous positioning and orienting of micrometer-scale components, with contact pushing used for coarse positioning and noncontact manipulation used for fine positioning.

Acknowledgment

The authors would like to thank the members of NanoRobotics Laboratory for all of their support and suggestions.

References

[1] D. Popa and E. Stephanou, "Micro and meso scale robotic assembly," *J. Manuf. Processes*, vol. 6, no. 1, pp. 52–71, 2004.

[2] L. Zhang, J. J. Abbott, L. Dong, B. E. Kratochvil, D. Bel, and B. J. Nelson, "Artificial bacterial flagella: Fabrication and magnetic control," *Appl. Phys. Lett.*, vol. 94, pp. 064107-1–064107-3, 2009.

[3] M. Dauge, M. Gauthier, and E. Piat, "Modelling of a planar magnetic micropusher for biological cell manipulations," *Sens. Actuators A*, vol. 138, pp. 239–247, 2007.

[4] S. Martel, C. Tremblay, S. Ngakeng, and G. Langlois, "Controlled manipulation and actuation of micro-objects with magnetotactic bacteria," *Appl. Phys. Lett.*, vol. 89, pp. 233904-1–233904-3, 2006.

[5] J. Abbott, Z. Nagy, F. Beyeler, and B. Nelson, "Robotics in the small, Part I: Microrobotics," *IEEE Robot. Autom. Mag.*, vol. 14, no. 2, pp. 92–103, Jun. 2007.

[6] M. Sitti, "Microscale and nanoscale robotics systems - Characteristics, state of the art, and grand challenges," *IEEE Robot. Autom. Mag.*, vol. 14, no. 1, pp. 53–60, Mar. 2007.

[7] P. J. Burke, "Nanodielectrophoresis: Electronic nanotweezers," in *Encyclopedia of Nanoscience and Nanotechnology, Encyclopedia of Nanoscience and Nanotechnology*, H. S. Nalwa, Ed. Stevenson Ranch, CA: American Scientific, vol. 10, pp. 1–19.

[8] K. C. Neuman and S. M. Block, "Optical trapping," *Rev. Sci. Instrum.*, vol. 75, no. 9, pp. 2787–2809, 2004.

[9] A. Masuda, T. Yamakawa, and L. Zimin, "Micromanipulation system based on local vibration," in *Proc. SICE Annu. Conf.*, 2008, pp. 1747–1750.

[10] K. Bohringer, V. Bhatt, B. Donald, and K. Goldberg, "Algorithms for sensorless manipulation using a vibrating surface," *Algorithmica*, vol. 26, no. 3–4, pp. 289–429, 2000.

[11] H. Becker and L. Locascio, "Polymer microfluidic devices," *Talanta*, vol. 56, no. 2, pp. 267–287, 2002.

[12] S. Chung and S. Cho, "On-chip manipulation of objects using mobile oscillating bubbles," *J. Micromech. Microeng.*, vol. 18, pp. 125024-1–125024-12, 2008.

[13] T. Deng, G. Whitesides, M. Radhakrishnan, G. Zabow, and M. Prentiss, "Manipulation of magnetic microbeads in suspension using micromagnetic systems fabricated with soft lithography," *Appl. Phys. Lett.*, vol. 78, no. 12, pp. 1775–1777, 2001.
[14] C. Liu, C. Chiang, C. Chang, and C. Liu, "A lobster-sniffing inspired actuator for manipulation of micro-objects via controlling local fluid," *Sens. Actuators A*, vol. 130–131, pp. 545–552, Aug. 2006.
[15] C. Pawashe, S. Floyd, and M. Sitti, "Modeling and experimental characterization of an untethered magnetic microrobot," *Int. J. Robot. Res.*, vol. 28, no. 8, pp. 1077–1094, Aug. 2009.
[16] R. Fearing, "Survey of sticking effects for micro parts handling," in *Proc. IEEE/RSJ Int. Conf. Intell. Robots Syst.*, 1995, vol. 2, pp. 212–217.
[17] F. Arai, D. Ando, T. Fukuda, Y. Nonoda, and T. Oota, "Micro manipulation based on micro physics - strategy based on attractive force reduction and stress measurement," in *Proc. IEEE/RSJ Int. Conf. Intell. Robots Syst.*, 1995, vol. 2, pp. 236–241.
[18] M. Gauthier, S. Regnier, P. Rougeot, and N. Chaillet, "Forces analysis for micromanipulations in dry and liquid media," *J. Micromech.*, vol. 3, no. 3–4, pp. 389–413, 2006.
[19] J. Israelachvili, *Intermolecular and Surface Forces*. London, U.K.: Academic, 1992.
[20] M. Sitti and H. Hashimototo, "Teleoperated touch feedback from the surfaces at the nanoscale: Modeling and experiments," *IEEE/ASME Trans. Mechatron.*, vol. 8, no. 2, pp. 287–298, Jun. 2003.
[21] D. Olsen and J. Osteraas, "The critical surface tension of glass," *J. Phys. Chem.*, vol. 68, no. 9, pp. 2730–2732, 1964.
[22] S. Rhee, "Surface energies of silicate glasses calculated from their wettability data," *J. Mater. Sci.*, vol. 12, pp. 823–824, 1977.
[23] M. Samuelsson and D. Kirchman, "Degradation of adsorbed protein by attached bacteria in relationship to surface hydrophobicity," in *Proc. Amer. Soc. Microbiol.*, 1990, pp. 3643–3648.
[24] T. Czerwiec, N. Renevier, and H. Michel, "Low-temperature plasma-assisted nitriding," *Surface Coatings Technol.*, vol. 131, pp. 267–277, 2000.
[25] M. Yuce and A. Demirel, "The effect of nanoparticles on the surface hydrophobicity of polystyrene," *Eur. Phys. J. B*, vol. 64, pp. 493–497, 2008.
[26] B. Munson, D. Young, and T. Okiishi, *Fundamentals of Fluid Mechanics*, 4th ed. New York: Wiley, 2002.
[27] J. Richardson and J. Harker, *Chemical Engineering*. vol. 2, 5th ed. London, U.K.: Butterworth and Heinemann, 2002.
[28] A. Goldman, R. Cox, and H. Brenner, "Slow viscous motion of a sphere parallel to a plane Wall II couette flow," *Chemical Eng. Sci.*, vol. 22, pp. 653–660, 1967.
[29] M. King and D. Leighton Jr., "Measurement of the inertial lift on a moving sphere in contact with a plane wall in a shear flow," *Phys. Fluids*, vol. 9, no. 5, pp. 1248–1255, 1997.

Steven Floyd (S'04) received the B.S. degree in mechanical engineering (*summa cum laude*) from Washington University, St. Louis, MO, in 2005 and the M.S. degree in mechanical engineering from Carnegie Mellon University, Pittsburgh, PA, in 2008. He is currently working toward the Ph.D. degree in mechanical engineering with the Department of Mechanical Engineering, Carnegie Mellon University.

His current research interests include robotic design, design and fabrication of microelectromechanical systems, serial and parallel micrometer-scale manipulation and assembly, the design, fabrication, and control of microrobotics, analog electronics design, and magnetic power transfer and actuation.

Mr. Floyd received the National Science Foundation Graduate Research Fellowship in 2005 and second prize at the World RoboCup Nanogram Demonstration in 2007.

Chytra Pawashe (S'09) received the B.S. and M.S. degrees in mechanical engineering from Carnegie Mellon University, Pittsburgh, PA, in 2006 and 2008, respectively. He is currently working toward the Ph.D. degree in mechanical engineering with the Department of Mechanical Engineering, Carnegie Mellon University.

His current research interests include micro/nanoscale manipulation and assembly, reconfigurable robotics, controls and automation, and bio-microdevices.

Mr. Pawashe received second prize at the World RoboCup Nanogram Demonstration in 2007.

Metin Sitti (S'94–M'00–SM'08) received the B.Sc. and M.Sc. degrees in electrical and electronics engineering from Bogazici University, Istanbul, Turkey, in 1992 and 1994, respectively, and the Ph.D. degree in electrical engineering from the University of Tokyo, Tokyo, Japan, in 1999.

He was a Research Scientist with the Department of Electrical Engineering and Computer Sciences, University of California, Berkeley, during 1999–2002. He is currently an Associate Professor with the Department of Mechanical Engineering and Robotics Institute, Carnegie Mellon University, Pittsburgh, PA. He is the Director of the NanoRobotics Laboratory, where his research interests include miniature mobile robots down to the micrometer-scale, biologically inspired micro/nanosystems, and micro/nanoscale manipulation and manufacturing systems.

Dr. Sitti has been the Adamson Career Faculty Fellow, since 2007, and has been nominated for the World Technology Award in 2009. He received the National Science Foundation CAREER award and the Carnegie Mellon Struminger Award in 2005. He was elected as the Distinguished Lecturer of the IEEE Robotics and Automation Society from 2006 to 2008. He received second prize at the World RoboCup Nanogram Demonstration in 2007, the best biomimetics paper award at the IEEE Robotics and Biomimetics Conference in 2004, the best paper award at the IEEE/RSJ International Conference on Intelligent Robots and Systems in 1998, and the best video award at the IEEE Robotics and Automation Conference in 2002. He is the Vice President of Technical Activities of the IEEE Nanotechnology Council for 2008–2010, the Co-Editor-in-Chief of the *Journal of Micro/Nano-Mechatronics*, and an Associate Editor for the IEEE TRANSACTIONS ON ROBOTICS.